

# Momentum dependence of spin-orbit interaction effects in single-layer and multi-layer transition metal dichalcogenides

R. Roldán, M.P. López-Sancho, F. Guinea

*Instituto de Ciencia de Materiales de Madrid, CSIC, c/ Sor Juana Ines de la Cruz 3, 28049 Cantoblanco, Madrid, Spain*

E. Cappelluti

*Istituto de Sistemi Complessi, U.O.S. Sapienza, CNR, v. dei Taurini 19, 00185 Roma, Italy*

J.A. Silva-Guillén, P. Ordejón

*ICN2 - Institut Catala de Nanociencia i Nanotecnologia, Campus UAB, 08193 Bellaterra, Spain and  
CSIC - Consejo Superior de Investigaciones Científicas, ICN2 Building, 08193 Bellaterra, Spain*

(Dated: November 18, 2014)

One of the main characteristics of the new family of two-dimensional crystals of semiconducting transition metal dichalcogenides (TMD) is the strong spin-orbit interaction, which makes them very promising for future applications in spintronics and valleytronics devices. Here we present a detailed study of the effect of spin-orbit coupling (SOC) on the band structure of single-layer and bulk TMDs, including explicitly the role of the chalcogen orbitals and their hybridization with the transition metal atoms. To this aim, we combine density functional theory (DFT) calculations with a Slater-Koster tight-binding model. Whereas most of the previous tight-binding models have been restricted to the K and K' points of the Brillouin zone (BZ), here we consider the effect of SOC in the whole BZ, and the results are compared to the band structure obtained by DFT methods. The tight-binding model is used to analyze the effect of SOC in the band structure, considering separately the contributions from the transition metal and the chalcogen atoms. Finally, we present a scenario where, in the case of strong SOC, the spin/orbital/valley entanglement at the minimum of the conduction band at Q can be probed and be of experimental interest in the most common cases of electron-doping reported for this family of compounds.

## I. INTRODUCTION

Transition metal dichalcogenides have emerged as a new family of layered materials with a number of remarkable electrical and optical properties.<sup>1</sup> Among them, single layers of the semiconducting compounds of the group-VIB  $MX_2$  (where  $M = \text{Mo, W}$  and  $X = \text{S, Se}$ ) are of special interest because they have a direct band gap in the visible range of the spectrum,<sup>2</sup> which is located in the K and K' points of the hexagonal BZ.<sup>3</sup> The absence of inversion symmetry in single layer samples lifts the spin degeneracy of the energy bands in the presence of SOC.<sup>4</sup> Interestingly, the spin splitting in inequivalent valleys must be opposite, as imposed by time reversal symmetry. This leads to the so called spin-valley coupling,<sup>5</sup> which has been studied theoretically<sup>6–10</sup> and observed experimentally.<sup>11–16</sup> Although the SOC splitting of the bands is particularly large in the valence band ( $\sim 150$  meV for  $\text{MoS}_2$  and  $\sim 400$  meV for  $\text{WS}_2$ ), a finite SOC splitting of the conduction band is also allowed by symmetry,<sup>17</sup> as confirmed by recent density functional theory calculations.<sup>18–24</sup> In addition, interlayer coupling plays here also a fundamental role. Indeed, the band structure dramatically changes from single-layer to multi-layer samples, involving a transition from a direct gap for single-layer samples to an indirect gap for multi-layer samples,<sup>3</sup> as it has been observed experimentally.<sup>2,25–27</sup>

Both numerical first-principles techniques and analytical approaches have been employed to investigate the role of the SOC in these materials. Within this context, the SOC has been mainly included in tight-binding (TB) models valid only in the low-energy range, where the presence of the  $p$ -

orbitals of the chalcogen atoms has been integrated out in an effective model (Refs. 5,28–32). Alternatively, DFT calculations can provide a more compelling description, but their complexity hampers the extraction of a simple model of the SOC. From a more general point of view, finally, most of the recent works on the effects of SOC in TMDs have been focused on single-layer samples, whereas fewer investigations have been devoted to the effect of SOC on the band structure of multi-layer and bulk samples. In particular, a complete TB model that can account for the effect of SOC in the whole BZ, including explicitly the  $p$ -orbitals of the chalcogen atoms, is lacking. Such a TB model is especially useful to study cases where DFT methods result too challenging computationally, as the effect of disorder, inhomogeneous strain, strong many-body interactions, etc.

In this paper we use a combination of TB and DFT calculations to provide a complete TB model, in the whole BZ, of the effects of SOC on the band structure of single-layer and multi-layer TMD taking explicitly into account the  $p$ -orbitals of the chalcogen atoms, and the atomic spin-orbit interaction on both the metal and chalcogen orbitals. The bands obtained from the TB model are compared to the corresponding DFT band structure for single layer and bulk  $\text{MoS}_2$  and  $\text{WS}_2$ . By considering the main orbital contribution at each relevant point of the BZ, we analyze the origin and main features of the SOC effects at the different band edges. Such model provides a useful base not only for the analytical investigation of the role of the SOC in the presence of local strain tuning the  $M$ - $X$  distance, but also for the investigation of the microscopical relevant spin-orbit processes. In particular, we show that the terms associated to second or-

der spin-flip processes of the SOC can be safely neglected for most of the cases of experimental interest. The TB model developed here is especially useful to analyze the effect of SOC at the so-called Q point of the BZ, which corresponds to the absolute minimum of the conduction band of multi-layer samples. We finally discuss also the peculiarities of the SOC in bilayer  $MX_2$ , for which the spin-valley-layer coupling could be exploit for future valleytronics applications.

The paper is organized as follows. In Section II we present the model for the single layer and bulk cases. The comparison between TB and DFT band structures considering the SOC effects, is illustrated in Section III for  $MoS_2$  and  $WS_2$ . Results are presented and discussed in Section IV. Finally the main findings are summarized and some conclusions are given in Section V.

## II. SPIN-ORBIT INTERACTION AND THE TIGHT-BINDING HAMILTONIAN

In this section we present the analytical structure of the TB Hamiltonians for single-layer and bulk TMD  $MX_2$  compounds including the SO interaction. Specific parameters for realistic materials will be provided in the next section, as well as a discussion of the physical consequences of the SOC.

### A. Single-layer case

The TMD  $MX_2$  are composed, in their bulk configuration, of two-dimensional  $X-M-X$  layers stacked on top of each other, coupled by weak van der Waals forces. The  $M$  atoms are ordered in a triangular lattice, each of them bonded to six  $X$  atoms located in the top and bottom layers, forming a sandwiched material. Our starting point will be a 11-band TB spinless model which, for the single-layer, considers the five  $d$  orbitals of the metal atom  $M$  and the three  $p$  orbitals for each of the two chalcogen atoms  $X$  in the top and bottom layer.<sup>3</sup> We can introduce a Hilbert base defined by the 11-fold vector:

$$\phi_i^\dagger = (p_{i,x,t}^\dagger, p_{i,y,t}^\dagger, p_{i,z,t}^\dagger, d_{i,3z^2-r^2}^\dagger, d_{i,x^2-y^2}^\dagger, d_{i,xy}^\dagger, d_{i,xz}^\dagger, d_{i,yz}^\dagger, p_{i,x,b}^\dagger, p_{i,y,b}^\dagger, p_{i,z,b}^\dagger), \quad (1)$$

where  $d_{i,\alpha}^\dagger$  creates an electron in the orbital  $\alpha$  of the  $M$  atom in the  $i$ -unit cell,  $p_{i,\alpha,t}^\dagger$  creates an electron in the orbital  $\alpha$  of the top ( $t$ ) layer atom  $X$  in the  $i$ -unit cell, and  $p_{i,\alpha,b}^\dagger$  creates an electron in the orbital  $\alpha$  of the bottom ( $b$ ) layer atom  $X$  in the  $i$ -unit cell. After an appropriate unitary transformation, the spinless (sl) representation of the single-layer (1L) Hamiltonian can be expressed in the block form

$$\hat{H}_{1L}^{sl}(\mathbf{k}) = \begin{pmatrix} \hat{H}_E & \hat{0}_{6 \times 5} \\ \hat{0}_{5 \times 6} & \hat{H}_O \end{pmatrix}, \quad (2)$$

where  $\hat{H}_E$  and  $\hat{H}_O$  are a  $6 \times 6$  and  $5 \times 5$  blocks with even (E) and odd (O) parity respectively upon the mirror inversion

$z \rightarrow -z$ , and  $\hat{0}_{m \times n}$  denotes  $m \times n$  zero matrices.<sup>3</sup> In particular,  $\hat{H}_E$  is built from hybridizations of the  $d_{xy}$ ,  $d_{x^2-y^2}$ ,  $d_{3z^2-r^2}$  orbitals of the metal  $M$  with the symmetric (antisymmetric) combinations of the  $p_x$ ,  $p_y$  ( $p_z$ ) orbitals of the top and bottom chalcogen atoms  $X$ . On the other hand, the odd block,  $\hat{H}_O$ , is made by hybridizations of the  $d_{xz}$  and  $d_{yz}$  orbitals of  $M$  with the antisymmetric (symmetric) combinations of the  $p_x$ ,  $p_y$  ( $p_z$ ) orbitals of the  $X$  atom in the top and bottom layers. Explicit expressions for all the matrix elements in terms of the Slater-Koster parameters were obtained in Ref. 3, and we notice that the  $6 \times 6$  even block  $\hat{H}_E$  contains the relevant orbital contribution for the states of the upper valence band and the lower conduction band.

In the context of the present TB model, we include the SOC term in the Hamiltonian by means of a pure atomic spin-orbit interaction acting on both the metal and chalcogen atoms. Explicitly we consider here the SOC given by:

$$\hat{H}^{SO} = \sum_a \frac{\lambda_a}{\hbar} \hat{\mathbf{L}}_a \cdot \hat{\mathbf{S}}_a, \quad (3)$$

where  $\lambda_a$ , the intra-atomic SOC constant, depends on the specific atom ( $a = M, X$ ).  $\hat{\mathbf{L}}_a$  is the atomic orbital angular momentum operator and  $\hat{\mathbf{S}}_a$  is the electronic spin operator.<sup>33-35</sup> It is convenient to use the representation

$$\hat{H}^{SO} = \sum_a \frac{\lambda_a}{\hbar} \left( \frac{\hat{L}_a^+ \hat{S}_a^- + \hat{L}_a^- \hat{S}_a^+}{2} + \hat{L}_a^z \hat{S}_a^z \right), \quad (4)$$

where (omitting now for simplicity the atomic index  $a$ ):

$$\hat{S}^+ = \begin{pmatrix} 0 & 1 \\ 0 & 0 \end{pmatrix}, \quad \hat{S}^- = \begin{pmatrix} 0 & 0 \\ 1 & 0 \end{pmatrix}, \quad \hat{S}^z = \frac{1}{2} \begin{pmatrix} 1 & 0 \\ 0 & -1 \end{pmatrix}. \quad (5)$$

In a similar way, the orbital angular momentum operator  $\hat{\mathbf{L}}$  acts on the states  $|l, m\rangle$  as

$$\begin{aligned} \hat{L}^\pm |l, m\rangle &= \hbar \sqrt{l(l+1) - m(m \pm 1)} |l, m \pm 1\rangle, \\ \hat{L}^z |l, m\rangle &= \hbar m |l, m\rangle, \end{aligned} \quad (6)$$

where  $l$  refers to the orbital momentum quantum number and  $m$  to its  $z$  component.

We choose the orbital basis set in the following manner:

$$\begin{aligned} |p_z\rangle &= |1, 0\rangle \\ |p_x\rangle &= -\frac{1}{\sqrt{2}}[|1, 1\rangle - |1, -1\rangle] \\ |p_y\rangle &= \frac{i}{\sqrt{2}}[|1, 1\rangle + |1, -1\rangle] \\ |d_{3z^2-r^2}\rangle &= |2, 0\rangle \\ |d_{xz}\rangle &= -\frac{1}{\sqrt{2}}[|2, 1\rangle - |2, -1\rangle] \\ |d_{yz}\rangle &= \frac{i}{\sqrt{2}}[|2, 1\rangle + |2, -1\rangle] \\ |d_{x^2-y^2}\rangle &= \frac{1}{\sqrt{2}}[|2, 2\rangle + |2, -2\rangle] \\ |d_{xy}\rangle &= -\frac{i}{\sqrt{2}}[|2, 2\rangle - |2, -2\rangle] \end{aligned} \quad (7)$$

We further simplify the problem by introducing the aforementioned symmetric (S) and antisymmetric (A) combination of the  $p$  orbitals of the top ( $t$ ) and bottom ( $b$ )  $X$  layers:

$$\begin{aligned} |p_{\alpha,S}\rangle &= \frac{1}{\sqrt{2}}[|p_{\alpha,t}\rangle + |p_{\alpha,b}\rangle], \\ |p_{\alpha,A}\rangle &= \frac{1}{\sqrt{2}}[|p_{\alpha,t}\rangle - |p_{\alpha,b}\rangle]. \end{aligned} \quad (8)$$

The total Hamiltonian, including the SO interaction for the single-layer, can be now written as

$$\hat{H}_{1L}(\mathbf{k}) = \hat{H}_{1L}^{\text{sl}}(\mathbf{k}) \otimes \mathbb{1}_2 + \hat{H}_{1L}^{\text{SO}}, \quad (9)$$

where the SOC term  $\hat{H}_{1L}^{\text{SO}}$  is

$$\hat{H}_{1L}^{\text{SO}} = \begin{pmatrix} \hat{M}^{\uparrow\uparrow} & \hat{M}^{\uparrow\downarrow} \\ \hat{M}^{\downarrow\uparrow} & \hat{M}^{\downarrow\downarrow} \end{pmatrix}, \quad (10)$$

and where

$$\hat{M}^{\sigma\sigma} = \begin{pmatrix} \hat{M}_{\text{EE}}^{\sigma\sigma} & \hat{0}_{6 \times 5} \\ \hat{0}_{5 \times 6} & \hat{M}_{\text{OO}}^{\sigma\sigma} \end{pmatrix}, \quad (11)$$

and

$$\hat{M}^{\sigma\bar{\sigma}} = \begin{pmatrix} \hat{0}_{6 \times 6} & \hat{M}_{\text{EO}}^{\sigma\bar{\sigma}} \\ \hat{M}_{\text{OE}}^{\sigma\bar{\sigma}} & \hat{0}_{5 \times 5} \end{pmatrix}. \quad (12)$$

Here we have chosen the spin notation  $\bar{\sigma} = \downarrow$  ( $\bar{\sigma} = \uparrow$ ) when  $\sigma = \uparrow$  ( $\sigma = \downarrow$ ).

The different blocks  $\hat{M}_{\text{EE}}^{\sigma\sigma}$ ,  $\hat{M}_{\text{OO}}^{\sigma\sigma}$ ,  $\hat{M}_{\text{EO}}^{\sigma\bar{\sigma}}$ ,  $\hat{M}_{\text{OE}}^{\sigma\bar{\sigma}}$ , that constitute the above  $22 \times 22$  matrix, are explicitly reported in the Appendix A. We notice here that, in the most general case, the SO interaction couples the E and O sectors of the  $22 \times 22$  TB matrix. Such mixing arises in particular from the spin-flip/spin-orbital processes associated with the transverse quantum fluctuation described by the first two terms of Eq. (4). The effective relevance of these terms can now be directly investigated in a simple way, pointing out the advantages of a TB model with respect to first-principles calculations. The explicit analysis of this issue is discussed in Section III. We anticipate here that the effects of the off-diagonal spin-flip terms result to be negligible for all the cases of interest here. *This is essentially due to the fact that such processes involve virtual transitions towards high-order energy states.*<sup>17</sup> At a very high degree of accuracy, we are thus justified in neglecting the spin-flip terms and retaining in (4) only the spin-conserving terms  $\propto \lambda_a \hat{L}_a^z \hat{S}_a^z$ . An immediate consequence of that is that the *even* and *odd* sectors of the Hamiltonian remain uncoupled, allowing us to restrict our analysis, for the low-energy states of the valence and conduction bands, only to the E sector.

## B. Bulk case

Once introduced the TB model for a single-layer in the presence of SOC, it is quite straightforward to construct a

corresponding theory for the bulk and bilayer systems by including the relevant inter-layer hopping terms in the Hamiltonian. Considering that the unit cell is now doubled, we can thus write the Hamiltonian for bulk  $MX_2$  in the presence of SOC in the matrix form:

$$\hat{H}_{\text{Bulk}}(\mathbf{k}) = \hat{H}_{\text{Bulk}}^{\text{sl}}(\mathbf{k}) \otimes \mathbb{1}_2 + \hat{H}_{\text{Bulk}}^{\text{SO}}, \quad (13)$$

which is a  $44 \times 44$  matrix due to the doubling of the unit cell with respect to the single-layer case discussed in Sec. II A.

Here  $\hat{H}_{\text{Bulk}}^{\text{sl}}(\mathbf{k})$  represents the spinless Hamiltonian for the bulk system,

$$\hat{H}_{\text{Bulk}}^{\text{sl}}(\mathbf{k}) = \begin{pmatrix} \hat{H}_1^{\text{sl}} & \hat{H}_{\perp,\text{Bulk}} \\ \hat{H}_{\perp,\text{Bulk}}^\dagger & \hat{H}_2^{\text{sl}} \end{pmatrix}, \quad (14)$$

where  $\hat{H}_i^{\text{sl}}$  describes the spinless Hamiltonian (i.e. in the absence of SOC) for the layer  $i = 1, 2$ , while  $\hat{H}_{\perp,\text{Bulk}}$  accounts for the  $11 \times 11$  Hamiltonian describing interlayer hopping between  $X$  atoms belonging to different layers. We remind that  $\hat{H}_2^{\text{sl}}$  is related to  $\hat{H}_1^{\text{sl}}$  through the following relation dictated by the lattice structure:<sup>3</sup>

$$\hat{H}_{2,\alpha,\beta}^{\text{sl}}(k_x, k_y) = P_\alpha P_\beta \hat{H}_{1,\alpha,\beta}^{\text{sl}}(k_x, -k_y), \quad (15)$$

where  $P_\alpha = +(-)1$  if the orbital  $\alpha$  has even (odd) symmetry with respect to  $y \rightarrow -y$ . Furthermore, the (spin-diagonal) interlayer term  $\hat{H}_{\perp,\text{Bulk}}$  can be written as:

$$\hat{H}_{\perp,\text{Bulk}}(\mathbf{k}) = \begin{pmatrix} \hat{I}_{\text{E}} \cos \zeta & \hat{I}_{\text{EO}} \sin \zeta \\ -\hat{I}_{\text{EO}}^\dagger \sin \zeta & \hat{I}_{\text{O}} \cos \zeta \end{pmatrix}, \quad (16)$$

where  $\zeta = k_z c/2$  ( $c$  being the vertical size of the unit cell in the bulk system), and where the matrices  $\hat{I}_{\text{E}}$ ,  $\hat{I}_{\text{O}}$  and  $\hat{I}_{\text{EO}}$  describe the inter-layer hopping between the  $p$  orbitals of the adjacent chalcogen atoms. One can notice that interlayer hopping leads, for an arbitrary wave-vector  $\mathbf{k}$ , to a mixture of the E and O sectors of the Hamiltonian, which is accounted for by the term  $\hat{I}_{\text{EO}}$  in (16).<sup>3</sup> The analysis is however simplified at specific high-symmetry points of the BZ, as we discuss below.<sup>50</sup>

Finally  $\hat{H}_{\text{Bulk}}^{\text{SO}}$  in Eq. (13) accounts for the spin-orbit coupling in the bulk system, and it can be written as:

$$\hat{H}_{\text{Bulk}}^{\text{SO}} = \begin{pmatrix} \hat{M}^{\uparrow\uparrow} & 0 & \hat{M}^{\uparrow\downarrow} & 0 \\ 0 & \hat{M}^{\uparrow\uparrow} & 0 & \hat{M}^{\uparrow\downarrow} \\ \hat{M}^{\downarrow\uparrow} & 0 & \hat{M}^{\downarrow\downarrow} & 0 \\ 0 & \hat{M}^{\downarrow\uparrow} & 0 & \hat{M}^{\downarrow\downarrow} \end{pmatrix}, \quad (17)$$

where both the spin-diagonal ( $\hat{M}^{\sigma\sigma}$ ) and spin-flip ( $\hat{M}^{\sigma\bar{\sigma}}$ ) processes induced by the atomic spin-orbit interaction are present.

Eqs. (13)-(17) provide the general basic framework for a deeper analysis in more specific cases. In particular, as already mentioned above, the spin-flip terms triggered by SOC can be substantially neglected for all the cases of interest without loosing accuracy. The total Hamiltonian (13) can thus be divided in two  $22 \times 22$  blocks  $\hat{H}_{\text{Bulk}}^{\sigma\sigma}(\mathbf{k})$  related by

the symmetry  $\hat{H}_{\text{Bulk}}^{\uparrow\uparrow}(\mathbf{k}) = \hat{H}_{\text{Bulk}}^{\downarrow\downarrow}(-\mathbf{k})$ . Further simplifications are available at specific symmetry points of the BZ. More specifically, we can notice that for  $k_z = 0$  the E and O sectors remain uncoupled. Focusing, at low-energies for the conduction and valence bands, only on the E sector, we can write

$$\hat{H}_{\text{Bulk,E}}(\mathbf{k}, k_z = 0) = \hat{H}_{\text{Bulk,E}}^{\text{sl}}(\mathbf{k}) + \hat{H}_{\text{Bulk,E}}^{\text{SO}}, \quad (18)$$

where

$$\hat{H}_{\text{Bulk,E}}^{\text{sl}}(\mathbf{k}) = \begin{pmatrix} \hat{H}_{\text{E},1} & \hat{I}_{\text{E}} & 0 & 0 \\ \hat{I}_{\text{E}}^\dagger & \hat{H}_{\text{E},2} & 0 & 0 \\ 0 & 0 & \hat{H}_{\text{E},1} & \hat{I}_{\text{E}} \\ 0 & 0 & \hat{I}_{\text{E}}^\dagger & \hat{H}_{\text{E},2} \end{pmatrix}, \quad (19)$$

and

$$\hat{H}_{\text{Bulk,E}}^{\text{SO}} = \begin{pmatrix} \hat{M}_{\text{EE}}^{\uparrow\uparrow} & 0 & 0 & 0 \\ 0 & \hat{M}_{\text{EE}}^{\uparrow\uparrow} & 0 & 0 \\ 0 & 0 & \hat{M}_{\text{EE}}^{\downarrow\downarrow} & 0 \\ 0 & 0 & 0 & \hat{M}_{\text{EE}}^{\downarrow\downarrow} \end{pmatrix}, \quad (20)$$

where the explicit expression of each block Hamiltonian is also reported in Appendix A.

### C. Bilayer

The Hamiltonian for the bilayer can also be derived in a very similar form as in the bulk case. In particular, we can write:

$$\hat{H}_{2\text{L}}(\mathbf{k}) = \hat{H}_{2\text{L}}^{\text{sl}}(\mathbf{k}) + \hat{H}_{2\text{L}}^{\text{SO}}. \quad (21)$$

Since we are considering intrinsic SOC, thus it is not affected by the interlayer coupling. Therefore we have  $\hat{H}_{2\text{L}}^{\text{SO}} = \hat{H}_{\text{Bulk}}^{\text{SO}}$ , where  $\hat{H}_{\text{Bulk}}^{\text{SO}}$  is defined in Eq. (20).

On the other hand, similar to the bulk case in Eq. (14), the spinless tight-binding term  $\hat{H}_{2\text{L}}^{\text{sl}}(\mathbf{k})$  for the bilayer case can be written as:

$$\hat{H}_{2\text{L}}^{\text{sl}}(\mathbf{k}) = \begin{pmatrix} \hat{H}_1^{\text{sl}} & \hat{H}_{\perp,2\text{L}} \\ \hat{H}_{\perp,2\text{L}}^\dagger & \hat{H}_2^{\text{sl}} \end{pmatrix}, \quad (22)$$

where now

$$\hat{H}_{\perp,2\text{L}}(\mathbf{k}) = \frac{1}{2} \begin{pmatrix} \hat{I}_{\text{E}} & \hat{I}_{\text{EO}} \\ -\hat{I}_{\text{EO}}^\dagger & \hat{I}_{\text{O}} \end{pmatrix}. \quad (23)$$

Note that Eq. (23) can be obtained as limiting case of Eq. (16) by setting  $\zeta = \pi/4$ , corresponding to the effective uncoupling of bilayer blocks.

### III. TIGHT-BINDING PARAMETERS AND COMPARISON WITH DFT CALCULATIONS

After having developed a suitable tight-binding model for single and multi-layer  $\text{MX}_2$  compounds, we compare in this

		MoS <sub>2</sub>	WS <sub>2</sub>
SOC	$\lambda_{\text{Mo}}$	0.075	0.215
	$\lambda_{\text{S}}$	0.052	0.057
Crystal Fields	$\Delta_0$	-1.512	-1.550
	$\Delta_1$	0.419	0.851
	$\Delta_2$	-3.025	-3.090
	$\Delta_p$	-1.276	-1.176
	$\Delta_z$	-8.236	-7.836
Intralayer Mo-S	$V_{pd\sigma}$	-2.619	-2.619
	$V_{pd\pi}$	-1.396	-1.396
Intralayer Mo-Mo	$V_{dd\sigma}$	-0.933	-0.983
	$V_{dd\pi}$	-0.478	-0.478
	$V_{dd\delta}$	-0.442	-0.442
Intralayer S-S	$V_{pp\sigma}$	0.696	0.696
	$V_{pp\pi}$	0.278	0.278
Interlayer S-S	$U_{pp\sigma}$	-0.774	-0.774
	$U_{pp\pi}$	0.123	0.123

TABLE I: Spin-orbit coupling  $\lambda_\alpha$  and tight-binding parameters for single-layer MoS<sub>2</sub> and WS<sub>2</sub> ( $\Delta_\alpha$ ,  $V_\alpha$ ) as obtained by fitting the low energy conduction and valence bands. Also shown are the interlayer hopping parameters  $U_\alpha$  relevant for bulk compounds. The Slater-Koster parameters for MoS<sub>2</sub> are taken from Ref. 3, and the SOC terms from Ref. 10 and 24. All hopping terms  $V_\alpha$ ,  $U_\alpha$ , crystal fields  $\Delta_\alpha$ , and spin-orbit coupling  $\lambda_\alpha$  are in units of eV.

section the band structure obtained by the TB model to the corresponding band structure obtained from DFT methods. An appropriate set of tight-binding parameters can be derived by fitting the low-energy dispersion of the conduction and valence bands of these compounds in the whole BZ, including the secondary minimum of the conduction band at the Q point, along the  $\Gamma$ -K line. The crystal field  $\Delta_1$  is obtained by fixing the minimum at K of the electronic bands belonging to the *odd* block to the same energy of the DFT calculations. The only left unknown parameters are thus the atomic spin-orbit constants  $\lambda_M$  and  $\lambda_X$  for the transition metal and for the chalcogen atom, respectively. We take the corresponding values from Ref. 10 and 24, and we list the full set of TB parameters for MoS<sub>2</sub> and WS<sub>2</sub> in Table I. Therefore, we can compare the resulting band structure for the full tight-binding model in the presence of SOC, with corresponding first-principles results including also spin-orbit interaction.

DFT calculations were performed using the SIESTA code.<sup>36,37</sup> The spin-orbit interaction is treated as in Ref. 38. We use the exchange-correlation potential of Ceperley-Alder<sup>39</sup> as parametrized by Perdew and Zunger.<sup>40</sup> We use also a split-valence double- $\zeta$  basis set including polarization functions.<sup>41</sup> The energy cutoff and the Brillouin zone sampling were chosen to converge the total energy. Lattice parameters for MoS<sub>2</sub> and WS<sub>2</sub> were chosen according to their experimental values, as reported in Refs. 42 and 43, and they

are listed in Table II.

The representative band structure for monolayer MoS<sub>2</sub> and WS<sub>2</sub>, as well as for the bulk counterpart, are shown in Fig. 1, for both DFT (dashed red lines) and TB calculations (solid blue lines). We observe that the TB model with the set of Slater-Koster parameters provided in Table I leads to a reasonable fitting of the DFT band structure. In particular we see that, for single layer samples [panels (a) and (b)] the edges of the valence band at K and  $\Gamma$ , as well as the edges of the conduction band at K and Q [which position is marked by a vertical dash in Fig. 1(a)] are properly captured by the TB model. The TB valence bands are less dispersive than the DFT bands in the intermediate regions between high symmetry points. The experimental bands measured by ARPES also seem to be flatter than the DFT bands, as it has been recently shown in Ref. 26. However it is important to notice that those experimental results for the band dispersion can be affected by the interaction between the  $MX_2$  crystals and the substrate, which is not considered neither in DFT calculations nor in the TB model. The TB band structure for bulk samples, shown in Fig. 1(c) and (d), have been obtained by adding *only* two extra Slater-Koster parameters,  $U_{pp\sigma}$  and  $U_{pp\pi}$ , which account for inter-layer hopping between  $p$  orbitals of the adjacent chalcogen atoms of different layers. The obtained band structure for the valence band reproduce reasonably well the DFT band structure, as well as the experimental band structure measured by ARPES,<sup>26</sup> and accounts for the direct- to indirect-gap transition when going from 1L to bulk materials.<sup>3</sup> As for the conduction band, the minimum at K is also captured by the TB model, but the energy of the minimum at Q does not agree with DFT results. The inclusion of hopping terms between  $M$  orbitals of different layers, as well as next nearest neighbor hopping terms, could improve such fitting.<sup>44</sup> However, we notice that no experimental measurements of the conduction band dispersion are available so far in the literature that could serve to validate the DFT and the TB results presented here.

In addition to the above remarks, a fundamental advantage of the TB model with respect to first-principles calculations is that it permits to investigate, in an analytical way, the relevance of the microscopic underlying processes. We have already mentioned above how transverse spin-flip fluctua-

	$a$	$u$	$c'$
MoS <sub>2</sub> 1L	3.16	1.586	—
MoS <sub>2</sub> 2L	3.16	1.586	6.14
MoS <sub>2</sub> Bulk	3.16	1.586	6.14
WS <sub>2</sub> 1L	3.153	1.571	—
WS <sub>2</sub> 2L	3.153	1.571	6.1615
WS <sub>2</sub> Bulk	3.153	1.571	6.1615

TABLE II: Lattice parameters used for DFT calculation for single-layer, bilayer and bulk MoS<sub>2</sub> and WS<sub>2</sub> systems, as taken from Refs. 42 and 43, respectively.  $a$  represents the  $M$ - $M$  atomic distance,  $u$  the internal vertical distance between the  $M$  plane and the  $X$  plane, and  $c'$  the distance between the  $M$  layers. In bulk systems the  $z$ -axis lattice parameter is given by  $c = 2c'$ . All values are in Å units.

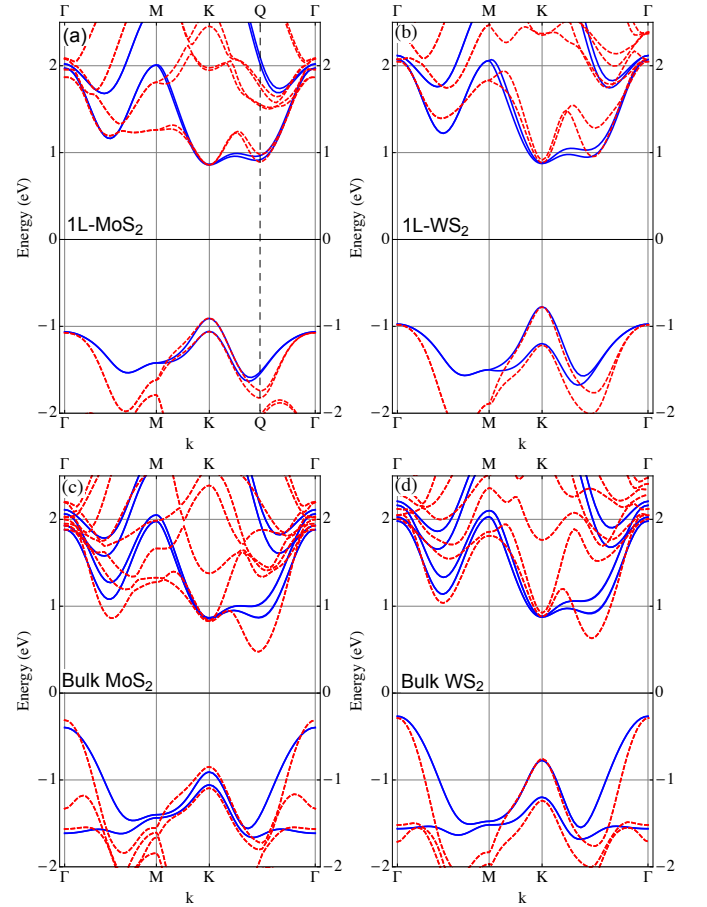


FIG. 1: Band structure of single-layer and bulk MoS<sub>2</sub> and WS<sub>2</sub> including SO interaction. Red dashed lines correspond to DFT calculations and solid blue lines to tight-binding calculations using the sets of parameters given in Table I. The vertical dashed line in panel (a) indicates the position of the minimum of the conduction band, referred in the text as Q.

tions play here a marginal role and they can be disregarded, making the overall modeling of the spin-orbit interaction extremely direct and simple. We can now explicitly address and quantify this issue by comparing in the TB model the band structures obtained by using the full SOC as described by Eq. (4) and the one obtained considering only the last spin-diagonal terms  $\hat{L}_a^z \hat{S}_a^z$ . The results are shown in Fig. 2 where we compare, for single-layer MoS<sub>2</sub> and WS<sub>2</sub>, the total band structure (red dashed lines) obtained by considering the full spin-orbit interaction (4) with the one obtained using the spin-conserving part [third term in Eq. (4)]. As we can see in Fig. 2(a) there is an almost perfect overlapping of the band structures for MoS<sub>2</sub> obtained including and neglecting the spin-flip terms, demonstrating the negligible role of these processes and the validity of the approximation. The effect is still weak but more noticeable for the case of WS<sub>2</sub> [Fig. 2(b)], due to the larger atomic SOC associated to the heavier W atoms, as compared to Mo.

Of special interest is the minimum of the conduction band

at the K point of the BZ: here, as discussed in Refs. 10,23,24, the competition between second order spin-flip processes associated with the transition metal atom  $M$  and first order (spin-conserving) processes of the chalcogen atom  $X$ , are responsible for the crossing/non crossing of the conduction bands in a very narrow region close to this K point.

#### IV. DISCUSSION

The TB model introduced in Sec. II, for single-layer and multi-layer compounds, and the specific Slater-Koster parameter set discussed in Sec. III provide a comprehensive tool for the study of the electronic properties and the entanglement between different degrees of freedom (spin, orbital, valley, layer, lattice) in these compounds in the presence of a relevant SOC acting both on the chalcogen  $X$  and on the transition metal atoms  $M$ . As we summarize in the present Section, such physics results to be relevant not only for the valence bands, whose band edge in the single layer materials is mainly built by the  $M$  orbitals  $d_{xy}$ ,  $d_{x^2-y^2}$ , but also for the conduction band and for the secondary extrema of both conduction and valence bands, whose energy can be effectively tuned by the interlayer coupling and by the spin-orbit interaction itself.

##### A. Spin-polarized pockets in the Fermi surfaces

The role of the SOC on the spin-orbital-valley entanglement at the band edge at K of the single-layer and bilayer compounds has been previously discussed in the literature, using mainly low-energy effective Hamiltonians focused on the role of the transition metal  $M$   $d$ -orbitals and of their corresponding spin-orbit coupling.<sup>5,8,28–32</sup> Such scenario can be

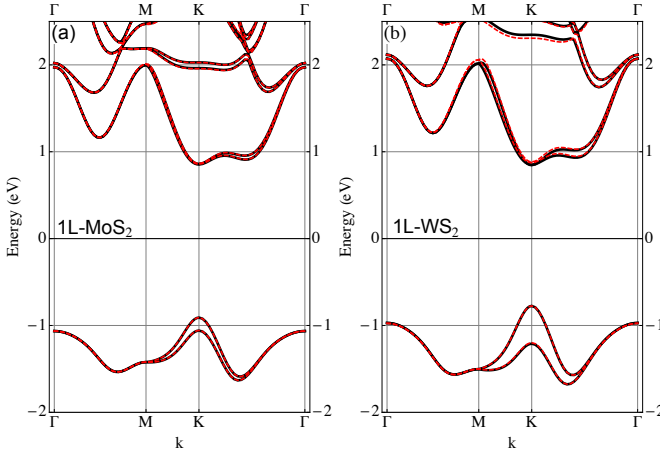


FIG. 2: Tight-binding band structure of single-layer MoS<sub>2</sub> (a) and WS<sub>2</sub> (b) including SO interaction. Red dashed lines corresponds to the TB bands including the whole SO coupling terms. Black solid lines correspond to the TB band structure including only the spin-conserving terms of the SO coupling.

now well reproduced by the present TB model and generalized to the whole BZ.

The spin-orbit coupling, in particular, is expected to be most relevant for the band edges of the valence band at the K point, whose orbital content is mainly associated with the  $d_{xy}$  and  $d_{x^2-y^2}$  orbitals of the transition metal. A large band splitting induced by the SOC is thus predicted in this case. Such feature is indeed well captured by the TB model. In Fig. 3(a) and (b) we show the Fermi surfaces obtained with the present TB model, including atomic SOC, for a finite hole-doping probing the valence band of both single-layer and bulk compounds. In order to point out the different physics occurring close to the different band edges at K and  $\Gamma$  points, we show here Fermi surfaces corresponding to a sizable negative Fermi energy cutting both edges at K and  $\Gamma$ . In particular, the central Fermi pocket located around  $\Gamma$  appears to be spin degenerate, for both single-layer and bulk systems since its orbital character is mainly due to the  $d_{3z^2-r^2}$  orbitals of  $M$  and to the  $p_z$  orbitals of  $X$ ,<sup>3</sup> both of them with  $L_z = 0$ . On the other hand, the pockets around K and K' are mainly due to the  $d_{x^2-y^2}$  and  $d_{xy}$  orbitals of the metal  $M$  (with  $|m| = 2$ ), plus a minor component of  $p_x$  and  $p_y$  orbitals of the chalcogen  $X$  (with  $|m| = 1$ ). This results in a finite SOC splitting of the valence band at the K and K' points, due mainly to first order spin-orbit coupling on the  $d$  orbitals of  $M$ . Furthermore, because of the lack of inversion symmetry in single layer samples (or in multi-layer samples with an odd number of layers), the spin degeneracy is lifted, presenting an opposite spin polarization on different valleys.<sup>5</sup> This feature is well reproduced by our model and shown in Fig. 3(a), where Fermi surfaces with main  $S_z = \uparrow$  character are denoted by solid blue lines, while Fermi surfaces with main  $S_z = \downarrow$  character are denoted by dashed blue lines. On the other hand, the Fermi surfaces of hole-doped bulk MoS<sub>2</sub>, for the same  $E_F$ , are shown in Fig. 3(b). Since the maximum of the valence band for the bulk compound, because of the interlayer coupling, is located at the  $\Gamma$  point [see the band structure of Fig. 1(c)], the central pocket in Fig. 3(b) is considerably larger than in Fig. 3(a) for single layer samples. The double Fermi surfaces around the K and K' points in 3(b) are spin degenerate, as imposed by inversion symmetry. A recent set of ARPES measurements for MoS<sub>2</sub> and MoSe<sub>2</sub><sup>45</sup> have shown the importance of the SOC in the band structure, obtaining experimental constant energy contours in very much agreement with those presented in Fig. 3(a) and (b).

Although smaller and less noticed,<sup>17–19,22–24</sup> a spin-valley coupling is present also for the conduction band edge of the single-layer systems at the K and K' points. It is important to remind here that the orbital character in these points of the BZ is mainly associated with the  $d_{3z^2-r^2}$  orbital (with  $m = 0$ ) of the transition metal  $M$ , but with a finite contribution from the  $p_x$  and  $p_y$  orbitals of the chalcogen, with  $m = \pm 1$ .<sup>3</sup> The spin-orbit coupling of the chalcogen atom  $X$ , mainly through the diagonal term  $L_X^z S_X^z$ , results thus in a smaller but finite splitting of the conduction band edge, as it can be also inferred by the Fermi surfaces for electron-doped single-layer compounds, as shown in Fig. 3(c). It is worth to stress that, although the resulting spin-induced splitting



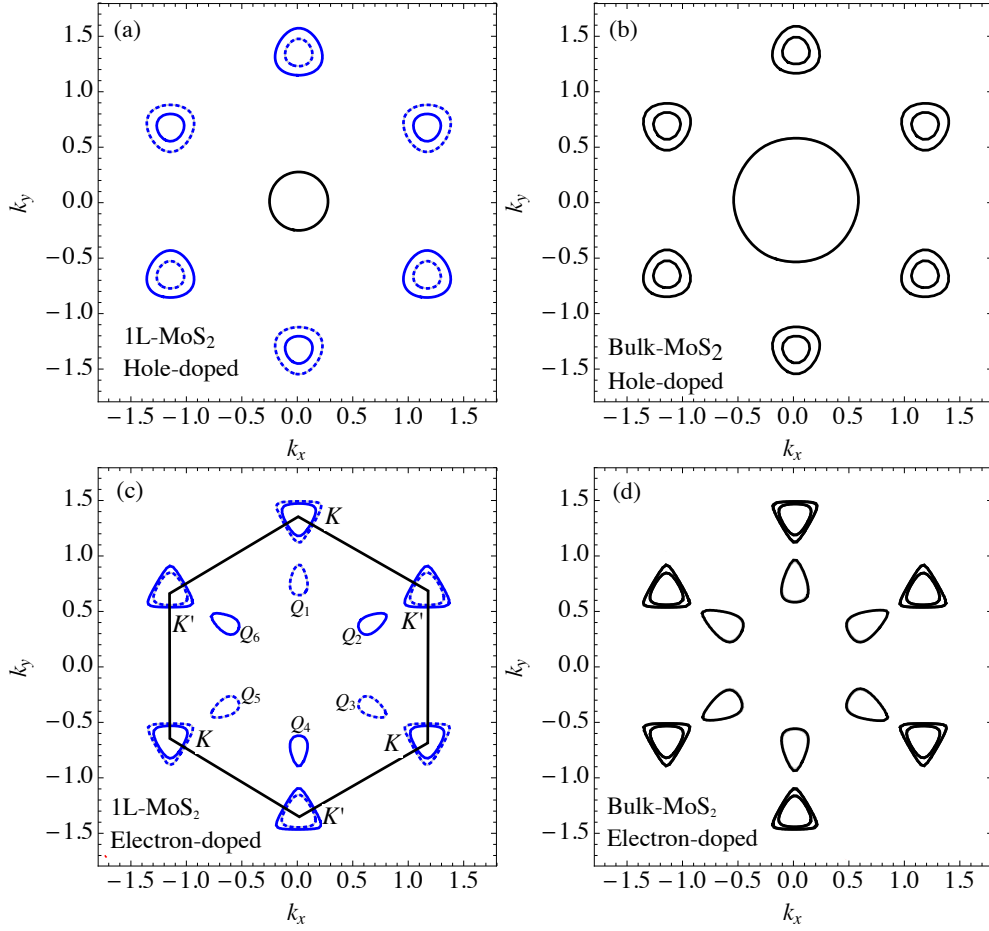


FIG. 3: Fermi surfaces of MoS<sub>2</sub>, obtained from the TB band structure. Panels (a) and (c) correspond to single-layer and panels (b) and (d) to the bulk. Top panels represent hole-doped systems, with the Fermi energy in the valence band (at  $E_F = -1.134$  eV), whereas bottom panels represent electron-doped systems, with the Fermi energy in the conduction band ( $E_F = 0.95$  eV). Energies are measured with respect to the zero of the TB Hamiltonian. The hexagonal 2D BZ is shown in (c) by the black solid lines. In panels (a) and (c), solid blue and dashed blue lines correspond to Fermi surfaces with main  $S_z = \uparrow$  and  $S_z = \downarrow$  polarization, respectively. Solid black lines indicate pockets which are degenerate in spin, like the central pocket in (a) (around the  $\Gamma$  point) and all the pockets in the Fermi surfaces of the bulk compound [panels (b) and (d)].

can be quite small, the entanglement between band splitting, spin and valley degrees appears to be quite strong, so that the lower band is  $\uparrow$  polarized and the upper band  $\downarrow$  polarized (or viceversa, depending on the valley). Note also that, although the atomic spin-orbit coupling due to the sulfur in MoS<sub>2</sub> or WS<sub>2</sub> is not very large, it can be of importance for Se compounds (with a larger atomic mass than sulfur), as MoSe<sub>2</sub> or WSe<sub>2</sub>. The role of the SOC on the chalcogen atom will be analyzed in more detail in Section IV B.

Finally, we can note that, as previously discussed in Ref. 4 using first principles calculations, the SOC induces a finite band splitting in single-layer systems also at the Q point, with a corresponding spin-polarization. Also this feature is nicely captured by our tight-binding model in the presence of atomic SOC on both chalcogen and transition metal atoms, as shown in Fig. 3(c) where we plot the Fermi surfaces of an electron-doped system with a Fermi level cutting only the lower conduction band at Q. As we can see,

the TB model is able not only to reproduce the band splitting, but also to point out a strong degree of entanglement in this point of the BZ, with Fermi pockets with a strong spin polarization, and with an alternating polarization of the entangled spin/valley/orbital degrees of freedom along the six inequivalent valleys.<sup>46</sup> On the microscopic ground, we can notice that the main orbital character of the conduction bands at the Q point is due to a roughly equal distribution of the  $d_{x^2-y^2}$  and  $d_{xy}$  orbitals of the transition metal  $M$ , and of the  $p_x$  and  $p_y$  orbitals of the chalcogen atom  $X$ . Given the presence of a large contribution from both  $p$ - and  $d$ -orbitals, we expect these states to stem from a strong hybridization between  $X$  and  $M$  atoms, and hence to be highly sensitive to uniform and local strains and lattice distortions.<sup>47</sup> In addition, it should be kept in mind that the minimum of the conduction band at Q becomes the effective band edge in bilayer and multilayer compounds (as well as in strained single-layer systems). These considerations thus suggest the

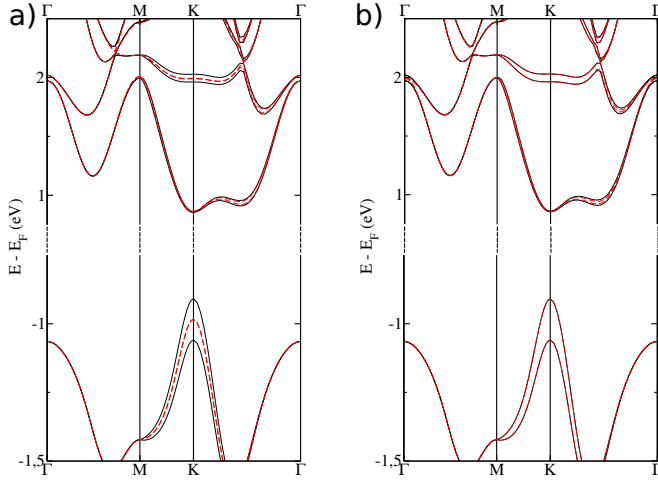


FIG. 4: Tight-binding band structure of MoS<sub>2</sub> including SOC. Solid black lines corresponds to the TB bands using  $\lambda_{\text{Mo}}$  and  $\lambda_{\text{S}}$  as given in Table I. Red dashed lines in (a) corresponds to  $\lambda_{\text{S}} = 0.052$  eV and  $\lambda_{\text{Mo}} = 0$ . Red dashed lines in (b) correspond to  $\lambda_{\text{Mo}} = 0.075$  eV and  $\lambda_{\text{S}} = 0$ .

minima of the conduction band at the Q point as the most promising states for tuning the spin/orbital/valley entanglement in these materials by means of strain engineering<sup>47</sup> or (in multilayer systems) by means of electric fields.<sup>14</sup>

### B. Effects of the chalcogen atom SOC on the band structure.

Most of the existing theoretical works have focused on the effects of the spin-orbit interaction associated with the transition metal atom. Less attention has been paid, in general, to the SOC induced by the chalcogen atom. As we have seen in the previous section, however, the role of the SOC can be remarkably relevant also at the Q point of the BZ, resulting in a strong spin/orbital/valley entanglement also in this point, with the advantage to be extremely sensitive to the  $M$ - $X$  hybridization and hence to the lattice effects. In addition, since the orbital content in this point is a mixture of  $d$  and  $p$  orbitals of the metal and the chalcogen atoms, the spin-orbit coupling is expected to be significantly driven not only by the  $d$ -orbital of the transition metal  $M$ , but also by the  $p$  orbitals of the chalcogen  $X$  atom. Tight-binding models can be quite useful to investigate this issue since we can easily tune the atomic SOC, keeping all the remaining Hamiltonian (Slater-Koster) parameters fixed, which permits to isolate the effects of the modified SOC without involving other structural and electronic changes. Figure 4 shows the effect of removing the SOC on either the Mo or the S atoms for the case of the single-layer of MoS<sub>2</sub>. While the splitting of the valence band at the K point is fully caused by the SOC on the transition metal, the contributions to the splitting of the conduction band at Q from Mo and S are comparable.

We can validate these findings by performing DFT calcu-

lations on the four compounds  $MX_2$  with  $M = \text{Mo}, \text{W}$  and  $X = \text{S}, \text{Se}$  (all of them done using the experimental structure). In the DFT calculation, we can also turn on and off the SOC on a particular species, by removing the SO component of the pseudopotential.<sup>48</sup> Fig. 5 shows the DFT results for the four compounds, including the SOC on all the atoms, and removing this coupling on either the chalcogen or the transition metal. In particular, the DFT results for MoS<sub>2</sub> shown in Fig. 5(a) agrees reasonably well with those of Fig. 4, signaling that the SOC splitting of the bands in the sulfur compounds is dominated by the contribution due to the transition metal atom.

The importance of the SOC of the chalcogen atom is expected to be more remarkable for heavier atoms, such as selenium, instead of sulfur. In Fig. 5(c) and (d) we show the DFT band structure for MoSe<sub>2</sub> and WSe<sub>2</sub>, isolating the contribution of the SOC due to the metal and to the chalcogen atoms. As expected, we observe that a relevant contribution to the SOC splitting of the bands is due to the Se atom. This can be seen by a noticeable splitting of the blue lines in Fig. 5(c) and (d) (for which the SOC due to the metal  $M$  has been switched off) which is governed by the spin-orbit interaction of the Se atoms. Interestingly, this effect is not relevant only at the Q point of the conduction band, but also at the K point of the valence band, for which the orbital weight of the  $p_x$  and  $p_y$  orbitals of Se is of *only*  $\sim 20\%$ .<sup>3</sup> We conclude that, although for the MoS<sub>2</sub> and WS<sub>2</sub> the effect of the SOC of the chalcogenides does not have much effect on the band structure, when S is changed by Se, the effect is much noticeable.

### C. Spin-Valley-Layer coupling in Bilayer $MX_2$

Of special interest is the case of bilayer TMD, corresponding to a stack of two single layers in-plane rotated by 180° with respect to each other, such that the transition metal atoms of one layer are above the chalcogen atoms of the other layer. The two layers are bound by means of weak van der Waals interactions. The inter-layer hopping of electrons between different layers leads to a strong modification of the band structure, driving a transition from a direct gap semiconductor in single-layer systems to an indirect gap semiconductor in bilayer and multi-layer compounds. The inter-layer hopping links mainly the  $p$  orbitals of the chalcogen atoms  $X$  of different layers.<sup>3</sup> The result of this hopping is a splitting of the maximum of the valence band at the  $\Gamma$  point, which becomes the effective valence band edge, as well as a splitting of the minimum of the conduction band at the Q point which becomes the absolute minimum of the conduction band. This situation is shown in Fig. 6, where we report the band structure of bilayer MoS<sub>2</sub> and WS<sub>2</sub> calculated by DFT methods. A qualitative similar feature is observed also in other bilayer compounds, as MoSe<sub>2</sub> or WSe<sub>2</sub>.

Contrary to single-layer  $MX_2$ , bilayer  $MX_2$  presents point-center inversion symmetry.<sup>14,16,49</sup> Therefore, as we have discussed for the bulk case, the corresponding band structure remains spin degenerate even in the presence of SOC. However, since the SOC Hamiltonian does not couple orbitals



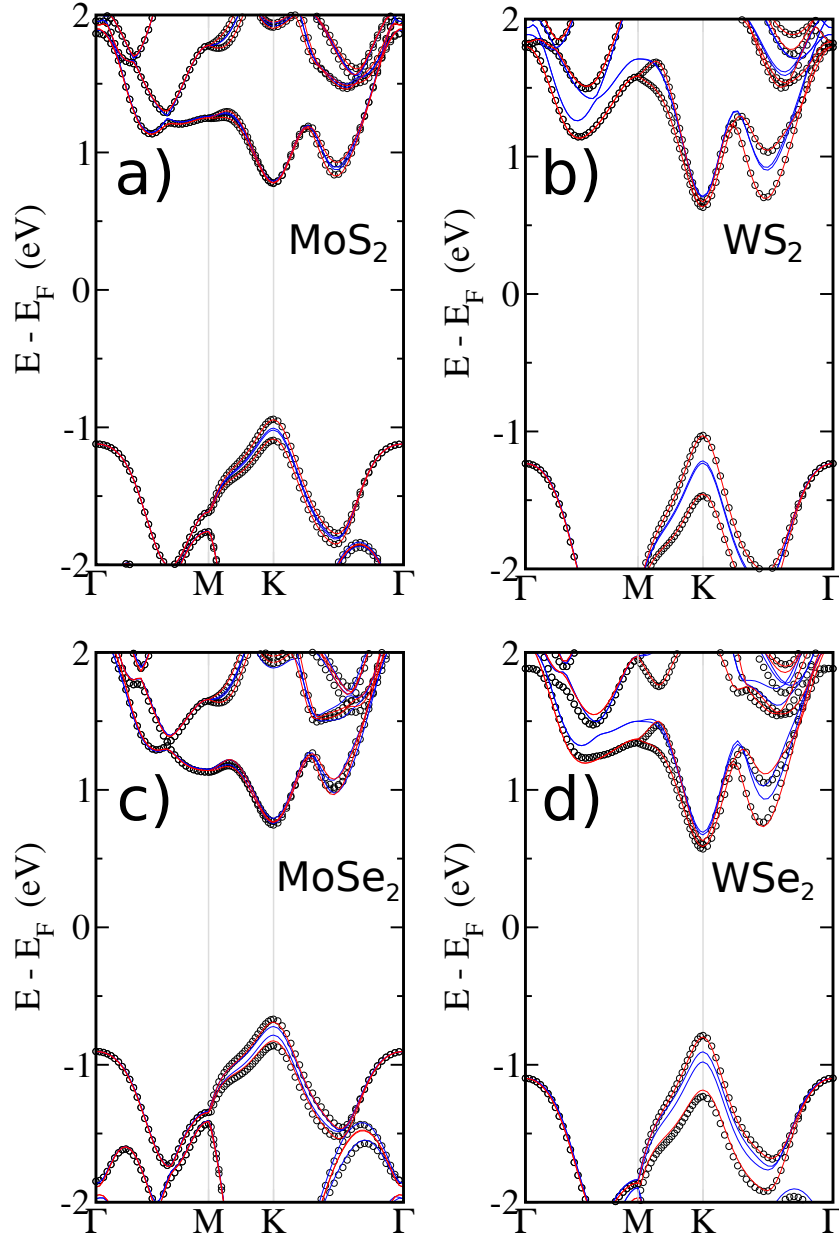


FIG. 5: DFT band structure of the four compounds  $\text{MoS}_2$ ,  $\text{WS}_2$ ,  $\text{MoSe}_2$  and  $\text{WSe}_2$ . Black circles show the results when the SOC on all the atoms are included. Red (blue) lines correspond to the removal of the SOC on the chalcogen (transition metal) atoms.

of different layers, each single band preserves a finite entanglement between spin, valley and the layer index. Such spin-valley-layer coupling has been discussed in Ref. 49, where the authors focused on the relevance of this effect at the K point of the valence band. Here we notice that the same effect occurs also for the conduction band, and it can be thus relevant for electron-doped samples. Indeed for slightly electron-doped bilayer  $\text{MoS}_2$  and  $\text{WS}_2$  the Fermi surface presents six pockets centered at the inequivalent Q valleys of the BZ, and no pockets at the K and K' valleys. Interestingly, the SOC for the TMD families with stronger spin-orbit interaction, like  $\text{WS}_2$  and  $\text{WSe}_2$ , can be larger than the inter-layer hopping, enhancing the spin/layer/valley en-

tanglement. Then, although inversion symmetry forces each Fermi pocket to be spin degenerate, the layer polarization makes that each layer contributes with opposite spin in alternating valleys. This property can be of interest for *valleytronics* devices: by partially filling only one of the two subbands at the Q point of the conduction band, one would have a situation in which the upper layer contributes to three of the six valleys with spin- $\uparrow$ , and with spin- $\downarrow$  to the other three valleys, whereas the opposite contribution is inferred from the bottom layer. This spin-valley coupling scenario resembles that of single-layer and bilayer  $\text{MX}_2$  discussed in the literature, but for electron-doped samples, which is the kind of doping most commonly reported for those materi-

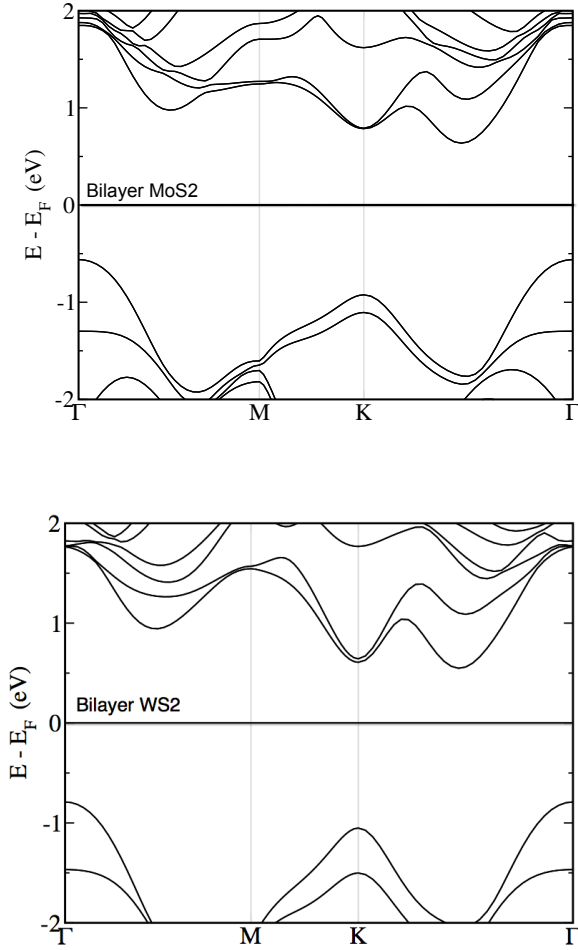


FIG. 6: Band structure of bilayer  $\text{MoS}_2$  and  $\text{WS}_2$  obtained from DFT calculations. The combined effect of inter-layer hopping and spin-orbit interaction drives the minimum of the conduction band to the Q point, and the maximum of the valence band to the  $\Gamma$  point (see text).

als. Although we have focused in this section in the most simple multi-layer compound, which is the bilayer  $\text{MX}_2$ , the physics discussed above applies also to any multi-layer TMD with an even number of layers, because they contain the same symmetry properties as that of bilayer  $\text{MX}_2$  discussed here.

## V. CONCLUSIONS

In conclusion, we have studied the effect of SOC in the band structure of TMD. We have used a tight-binding model, valid for single-layer samples as well as for multi-layer samples, which includes the SO interaction of both, the transition metal and the chalcogen atoms. The band structure obtained from the TB model has been compared to DFT calculations for  $\text{MoS}_2$  and  $\text{WS}_2$ . Based on the orbital character

at each relevant point of the Brillouin zone, we have discussed the origin and main features of the SOC effects at the different band edges. In particular we have found that, for the cases of interest here, spin-flip processes are negligible in the SOC Hamiltonian. This allows to highly simplify the model, making possible to construct a reduced TB Hamiltonian which contains the orbital character and SOC which is relevant for the description of the system around the gap. Special attention has been paid to the role of the SOC associated to the chalcogen atom. In fact, whereas most of the previous works has focused on the SOC associated to the metal atom (which is indeed the responsible for the large splitting of the valence band at the K point) here we have shown that the SOC associated to the chalcogen atom may be important at the Q point of the conduction band, and at the K point of the valence band, especially for  $\text{MoSe}_2$  and  $\text{WSe}_2$ . Finally, we have considered the effect of SOC in bilayer TMD. Whereas for single-layer  $\text{MX}_2$  inversion asymmetry leads to spin-valley coupling, the band edges of bilayer TMD are spin degenerate. However, since inter-layer hopping conserves the spin, the spin physics can be exploited in bilayer  $\text{MX}_2$  due to spin-valley-layer coupling. Whereas this issue has been recently studied in detail for hole-doped samples,<sup>49</sup> here we have argued that a similar effect can be expected for slightly electron-doped samples.

## Acknowledgments

We thank H. Ochoa and S. Gallego for useful discussions. R.R., M.P.L.-S. and F.G. acknowledge financial support from MINECO, Spain, through grant FIS2011-23713, and the European Union, through grant 290846. R. R. acknowledges financial support from the Juan de la Cierva Program (MINECO, Spain). E.C. acknowledges support from the European project FP7-PEOPLE-2013-CIG “LSIE\_2D” and Italian National Miur Prin project 20105ZZTSE. J.A.S.-G. and P.O. acknowledge support from Spanish MINECO (Grants No. FIS2012-37549-C05-02 with joint financing by FEDER Funds from the European Union, and No. CSD2007-00050). J.A.S.-G. was supported by an FPI Fellowship from MINECO. The authors thankfully acknowledges the computer resources, technical expertise and assistance provided by the Red Española de Supercomputación.

## Appendix A: SOC Hamiltonian

In this appendix we provide the explicit expression of the matrices  $\hat{M}_{EE}^{\sigma\sigma}$ ,  $\hat{M}_{OO}^{\sigma\sigma}$ ,  $\hat{M}_{EO}^{\sigma\sigma}$ ,  $\hat{M}_{OE}^{\sigma\sigma}$ , describing the local atomic spin-orbit interaction on both  $M$  and  $X$  atoms. We have:

$$\hat{M}_{EE}^{\uparrow\uparrow} = \begin{pmatrix} 0 & 0 & 0 & 0 & 0 & 0 \\ 0 & 0 & -i\lambda_M & 0 & 0 & 0 \\ 0 & i\lambda_M & 0 & 0 & 0 & 0 \\ 0 & 0 & 0 & 0 & -i\lambda_X/2 & 0 \\ 0 & 0 & 0 & i\lambda_X/2 & 0 & 0 \\ 0 & 0 & 0 & 0 & 0 & 0 \end{pmatrix} \quad (\text{A1})$$

$$\hat{M}_{EE}^{\downarrow\downarrow} = -\hat{M}_{EE}^{\uparrow\uparrow}, \quad (\text{A2})$$

$$\hat{M}_{OO}^{\uparrow\uparrow} = \frac{1}{2} \begin{pmatrix} 0 & -i\lambda_M & 0 & 0 & 0 \\ i\lambda_M & 0 & 0 & 0 & 0 \\ 0 & 0 & 0 & -i\lambda_X & 0 \\ 0 & 0 & i\lambda_X & 0 & 0 \\ 0 & 0 & 0 & 0 & 0 \end{pmatrix}, \quad (\text{A3})$$

$$\hat{M}_{OO}^{\downarrow\downarrow} = -\hat{M}_{OO}^{\uparrow\uparrow}, \quad (\text{A4})$$

$$\hat{M}_{EO}^{\uparrow\downarrow} = \frac{1}{2} \begin{pmatrix} -\sqrt{3}\lambda_M & i\sqrt{3}\lambda_M & 0 & 0 & 0 \\ \lambda_M & i\lambda_M & 0 & 0 & 0 \\ -i\lambda_M & \lambda_M & 0 & 0 & 0 \\ 0 & 0 & 0 & 0 & \lambda_X \\ 0 & 0 & 0 & 0 & -i\lambda_X \\ 0 & 0 & -\lambda_X & i\lambda_X & 0 \end{pmatrix} \quad (\text{A5})$$

$$\hat{M}_{OE}^{\downarrow\uparrow} = \left( \hat{M}_{EO}^{\uparrow\downarrow} \right)^\dagger, \quad (\text{A6})$$

$$\hat{M}_{EO}^{\downarrow\uparrow} = \frac{1}{2} \begin{pmatrix} \sqrt{3}\lambda_M & i\sqrt{3}\lambda_M & 0 & 0 & 0 \\ -\lambda_M & i\lambda_M & 0 & 0 & 0 \\ -i\lambda_M & -\lambda_M & 0 & 0 & 0 \\ 0 & 0 & 0 & 0 & -\lambda_X \\ 0 & 0 & 0 & 0 & -i\lambda_X \\ 0 & 0 & \lambda_X & i\lambda_X & 0 \end{pmatrix} \quad (\text{A7})$$

and

$$\hat{M}_{OE}^{\uparrow\downarrow} = \left( \hat{M}_{EO}^{\downarrow\uparrow} \right)^\dagger, \quad (\text{A8})$$

In the above matrices we have used the short notation  $\lambda_M$  for the SOC of the metal (Mo or W) and  $\lambda_X$  for the SOC of the chalcogen (S or Se).

- 
- <sup>1</sup> Q. H. Wang, K. Kalantar-Zadeh, A. Kis, J. N. Coleman, and M. S. Strano, *Nature Nanotech.* **7**, 699 (2012).
- <sup>2</sup> K. F. Mak, C. Lee, J. Hone, J. Shan, and T. F. Heinz, *Phys. Rev. Lett.* **105**, 136805 (2010).
- <sup>3</sup> E. Cappelluti, R. Roldán, J. A. Silva-Guillén, P. Ordejón, and F. Guinea, *Phys. Rev. B* **88**, 075409 (2013).
- <sup>4</sup> Z. Y. Zhu, Y. C. Cheng, and U. Schwingenschlögl, *Phys. Rev. B* **84**, 153402 (2011).
- <sup>5</sup> D. Xiao, G.-B. Liu, W. Feng, X. Xu, and W. Yao, *Phys. Rev. Lett.* **108**, 196802 (2012).
- <sup>6</sup> W. Feng, Y. Yao, W. Zhu, J. Zhou, W. Yao, and D. Xiao, *Phys. Rev. B* **86**, 165108 (2012).
- <sup>7</sup> W.-Y. Shan, H.-Z. Lu, and D. Xiao, *Phys. Rev. B* **88**, 125301 (2013).
- <sup>8</sup> H. Rostami, A. G. Moghaddam, and R. Asgari, *Phys. Rev. B* **88**, 085440 (2013).
- <sup>9</sup> F. Rose, M. O. Goerbig, and F. Piéchon, *Phys. Rev. B* **88**, 125438 (2013).
- <sup>10</sup> G.-B. Liu, W.-Y. Shan, Y. Yao, W. Yao, and D. Xiao, *Phys. Rev. B* **88**, 085433 (2013).
- <sup>11</sup> T. Cao, G. Wang, W. Han, H. Ye, C. Zhu, J. Shi, Q. Niu, P. Tan, E. Wang, B. Liu, et al., *Nature Commun.* **3**, 887 (2012).
- <sup>12</sup> H. Zeng, J. Dai, W. Yao, D. Xiao, and X. Cui, *Nature Nanotech.* **7**, 490 (2012).
- <sup>13</sup> K. F. Mak, K. He, J. Sahn, and T. F. Heinz, *Nature Nanotech.* **7**, 494 (2012).
- <sup>14</sup> S. Wu, J. S. Ross, G.-B. Liu, G. Aivazian, A. Jones, Z. Fei, W. Zhu, D. Xiao, W. Yao, D. Cobden, et al., *Nature Physics* **9**, 149 (2013).
- <sup>15</sup> Q. Wang, S. Ge, X. Li, J. Qiu, Y. Ji, J. Feng, and D. Sun, *ACS Nano* **7**, 11087 (2013).
- <sup>16</sup> H. Zeng, G.-B. Liu, J. Dai, Y. Yan, B. Zhu, R. He, L. Xie, S. Xu, X. Chen, W. Yao, et al., *Scientific Reports* **3**, 1608 (2013).
- <sup>17</sup> H. Ochoa and R. Roldán, *Phys. Rev. B* **87**, 245421 (2013).
- <sup>18</sup> T. Cheiwchanchamnangij and W. R. L. Lambrecht, *Phys. Rev. B* **85**, 205302 (2012).
- <sup>19</sup> K. Kośmider and J. Fernández-Rossier, *Phys. Rev. B* **87**, 075451 (2013).
- <sup>20</sup> A. Molina-Sánchez, D. Sangalli, K. Hummer, A. Marini, and L. Wirtz, *Phys. Rev. B* **88**, 045412 (2013).
- <sup>21</sup> Y. Song and H. Dery, *Phys. Rev. Lett.* **111**, 026601 (2013).
- <sup>22</sup> A. Kormányos, V. Zólyomi, N. D. Drummond, P. Rakyta, G. Burkard, and V. I. Fal'ko, *Phys. Rev. B* **88**, 045416 (2013).
- <sup>23</sup> A. Kormányos, V. Zólyomi, N. D. Drummond, and G. Burkard, *Phys. Rev. X* **4**, 011034 (2014).
- <sup>24</sup> K. Kośmider, J. W. González, and J. Fernández-Rossier, *Phys. Rev. B* **88**, 245436 (2013).
- <sup>25</sup> W. Zhao, R. M. Ribeiro, M. Toh, A. Carvalho, C. Kloc, A. H. Castro Neto, and G. Eda, *ArXiv e-prints* (2013), 1309.0923.
- <sup>26</sup> W. Jin, P.-C. Yeh, N. Zaki, D. Zhang, J. T. Sadowski, A. Al-Mahboob, A. M. van der Zande, D. A. Chenet, J. I. Dadap, I. P. Herman, et al., *Phys. Rev. Lett.* **111**, 106801 (2013).
- <sup>27</sup> Y. Zhang, T.-R. Chang, B. Zhou, Y.-T. Cui, H. Yan, Z. Liu, F. Schmitt, J. Lee, R. Moore, Y. Chen, et al., *Nature Nanotechnology* **9**, 111 (2014).
- <sup>28</sup> X. Li, F. Zhang, and Q. Niu, *Phys. Rev. Lett.* **110**, 066803 (2013).
- <sup>29</sup> J. Klinovaja and D. Loss, *Phys. Rev. B* **88**, 075404 (2013).
- <sup>30</sup> L. Wang and M. Wu, *Physics Letters A* **378**, 1336 (2014).
- <sup>31</sup> M. A. Cazalilla, H. Ochoa, and F. Guinea, *ArXiv e-prints* (2013), 1311.6650.
- <sup>32</sup> M. O. Goerbig, G. Montambaux, and F. Piéchon, *EPL (Europhysics Letters)* **105**, 57005 (2014).
- <sup>33</sup> S. Gallego and M. Munoz, *Surface science* **423**, 324 (1999).
- <sup>34</sup> L. Chico, M. P. López-Sancho, and M. C. Muñoz, *Phys. Rev. Lett.* **93**, 176402 (2004).
- <sup>35</sup> D. Huertas-Hernando, F. Guinea, and A. Brataas, *Phys. Rev. B* **74**, 155426 (2006).
- <sup>36</sup> J. Soler, E. Artacho, J. Gale, A. García, J. Junquera, P. Ordejón, and D. Sánchez-Portal, *J. Phys.: Condens. Matter* **14**, 2745 (2002).
- <sup>37</sup> E. Artacho, E. Anglada, O. Dieguez, J. Gale, A. García, J. Junquera, R. Martin, P. Ordejón, J. M. Pruneda, D. Sánchez-Portal, et al., *J. Phys.: Condens. Matter* **20**, 064208 (2008).
- <sup>38</sup> L. Fernández-Seivane, M. Oliveira, S. Sanvito, and J. Ferrer, *J. Phys.: Condens. Matter* **18**, 7999 (2006).

- <sup>39</sup> D. Ceperley and B. J. Alder, Phys. Rev. Lett. **45**, 566 (1980).
- <sup>40</sup> P. Perdew and A. Zunger, Phys. Rev. B **23**, 5048 (1981).
- <sup>41</sup> E. Artacho, D. Sánchez-Portal, P. Ordejón, A. García, and J. Soler, Phys. Status Solidi B **215**, 809 (1999).
- <sup>42</sup> R. A. Bromley, R. B. Murray, and A. D. Yoffe, J. Phys. C: Solid State Phys. **5**, 759 (1972).
- <sup>43</sup> W. Schutte, J. Boer, and F. Jellinek, J. Solid State Chem. **70**, 207 (1987).
- <sup>44</sup> We notice that the TB parameters used in this work lead to a trigonal warping of the conduction band which is rotated  $\pi/3$  with respect to the DFT bands. This fact does not affect the results discussed here.
- <sup>45</sup> N. Alidoust, G. Bian, S.-Y. Xu, R. Sankar, M. Neupane, C. Liu, I. Belopolski, D.-X. Qu, J. D. Denlinger, F.-C. Chou, et al., ArXiv e-prints (2013), 1312.7631.
- <sup>46</sup> H. Yuan, X. Wang, B. Lian, H. Zhang, X. Fang, B. Shen, G. Xu, Y. Xu, S.-C. Zhang, H. Y. Hwang, et al., ArXiv e-prints (2014), 1403.2696.
- <sup>47</sup> A. Castellanos-Gomez, R. Roldán, E. Cappelluti, M. Buscema, F. Guinea, H. S. J. van der Zant, and G. A. Steele, Nano Letters **13**, 5361 (2013).
- <sup>48</sup> L. Kleinman, Physical Review B **21** (1980).
- <sup>49</sup> Z. Gong, G.-B. Liu, H. Yu, D. Xiao, X. Cui, X. Xu, and W. Yao, Nature Communications **4** (2013).
- <sup>50</sup> See Ref. 3 for an explicit expression of all the matrix elements of the Hamiltonian (14).